Supersonic wave propagation in active non-Hermitian acoustic metamaterials

Kangkang Wang,[1] Felix Langfeldt,[2,*] Chen Shen,[3] Haishan Zou,[1] Sipei Zhao,[4] Jing Lu,[1,†] and Lea Sirota[5,‡]

[1] *Key Laboratory of Modern Acoustics, Ministry of Education (MOE), Institute of Acoustics, Department of Physics, Nanjing University, Nanjing 210093, People's Republic of China*
[2] *Institute of Sound and Vibration Research, University of Southampton, University Road, Highfield, Southampton SO17 1BJ, United Kingdom*
[3] *Department of Mechanical Engineering, Rowan University, Glassboro, New Jersey 08028, USA*
[4] *Centre for Audio, Acoustics and Vibration, Faculty of Engineering and IT, University of Technology Sydney, Ultimo, New South Wales 2007, Australia*
[5] *School of Mechanical Engineering, Tel Aviv University, Tel Aviv 69978, Israel*

(Received 21 April 2025; revised 23 August 2025; accepted 26 August 2025; published 23 September 2025)

Obtaining a group velocity higher than the speed of sound in a waveguide is a challenging task in acoustic wave engineering. Even more challenging is to achieve this velocity increase without any intervention with the waveguide profile, such as narrowing or widening, and particularly without interfering with the passage by flexible inclusions, either passive or active. Here, we approach this problem by invoking concepts from non-Hermitian physics, and imposing them using active elements that are smoothly sealed within the waveguide wall. In a real-time feedback operation, the elements induce local pressure gain and loss, as well as nonlocal pressure integration couplings. We employ a dedicated balancing between the control parameters, derived from lattice theory and adjusted to the waveguide system, to drive the dynamics into a stable parity-time-symmetric regime. We demonstrate the accelerated propagation of a wave packet both numerically and experimentally in an air-filled waveguide and discuss the trade-off between stabilization and the achievable velocity increase. Our work prepares the ground for advanced forms of wave transmission in continuous media, enabled by short- and long-range active couplings, created via embedded real-time feedback control.

DOI: 10.1103/zs92-qr17

I. INTRODUCTION

Non-Hermitian systems, in which interactions and exchange of energy with the surrounding environment are allowed, have been shown to exhibit unique properties in recent years [1,2]. Their effective non-Hermitian Hamiltonians endow exceptional properties and topologies that go beyond those of conventional Hermitian counterparts. A prime example is parity-time ($\mathcal{PT}$) symmetry and the emergence of exceptional points (EPs), which have garnered great research interest [3,4]. The eigenstates of these $\mathcal{PT}$-symmetric systems coalesce in the parameter space, and real eigenvalues are possible with non-self-adjoint Hamiltonians. Initially a purely mathematical model [5,6], the concept was later successfully tested in photonic systems with balanced loss and gain potentials due to the equivalence between the paraxial electromagnetic wave equation and the Schrödinger equation [7]. Since then, numerous $\mathcal{PT}$-symmetry and EP-related effects have been discovered, which have suggested new functionalities and applications by tailoring the complex energy profile of the systems under study, including single-mode lasers [8], enhanced sensitivity [9], unidirectional invisible cloaking [10,11], and so on.

In the field of acoustics and elastodynamics, researchers have studied similar concepts and revealed a plethora of intriguing phenomena [12–18]. Because of the absence of natural gain materials, a common approach is to implement an equivalent model with only lossy or lossless media, leaving part of the parameter space untapped. Although these systems are successful in terms of constructing complex effective Hamiltonians, recent studies have suggested that certain effects can only be induced by real gain-loss modulations [19–21]. The use of gain media introduces external energy and broadens the utility of the parameter space. Several previous case studies have

*Contact author: f.langfeldt@soton.ac.uk
†Contact author: lujing@nju.edu.cn
‡Contact author: leabeilkin@tauex.tau.ac.il

implemented real gain media using different techniques, such as electrothermoacoustic coupling [22,23], background airflow [24], energy injection [25,26], or active-control elements [27,28]. Nevertheless, the non-Hermitian phenomena demonstrated so far have been focused mostly on the property of nonreciprocity and less on the control of the wave-propagation velocity. In addition, the common realizations of active couplings—in particular, in acoustic waveguides—involve either alternations of the waveguide geometry or placement of the actuators in the waveguide cross section [27,29,30].

In this work, we address spatially continuous media, such as acoustic waveguides, hybridized with discretely spanned active elements, which are seamlessly embedded in the waveguide wall. We program these elements to actively control the wave-propagation velocity in a plain waveguide with a uniform cross section. This is useful for applications for which the passage of fluid through the waveguide cannot be blocked. Motivated by control schemes for purely discrete $\mathcal{PT}$-symmetric media, such as lattices [31,32], we derive the required couplings to speed up wave-packet propagation in the waveguide. Specifically, the active units control the on-site loss and gain profiles, as well as the couplings between the units, to create an effective $\mathcal{PT}$-symmetric system. Utilizing the concept of feedback-based media [30,33–41], we realize these couplings in a real-time closed-loop process.

At the first stage, we design a theoretical model to describe the controlled waveguide. Then, we suggest an analogous discrete model of a mass-spring lattice, and derive the relation between the control parameters that lead to a group velocity increase in the lattice and at the same time guarantee its dynamical stability. Mapping back to the waveguide system, we obtain the required control parameters therein. Despite the differences between purely discrete and hybrid continuous-discrete systems (e.g., due to time delays or near-field effects), we show that a faster group velocity compared to the background medium is possible in the waveguide system with judiciously tailored feedback-modulation profiles.

Owing to the central role that stability plays in actively controlled wave systems [42], we derive the theoretical criteria for stable wave dynamics in the metamaterial so that the wave amplitude is not growing during the propagation. We confirm our theoretical predictions of obtaining a group velocity higher than the speed of sound in air by carrying out experiments in an acoustic waveguide and we discuss the limitations of the achievable stability in the actual system. Our results showcase the implementation of active acoustic wave control in combination with $\mathcal{PT}$-symmetry to support stable faster-than-sound dynamic pulse transmission. The work facilitates the spatiotemporal modulation of signals with real-time tuning capabilities and may find applications in acoustic communication and more.

II. TARGET WAVEGUIDE MODEL

We consider an acoustic waveguide that supports propagation of sound pressure waves p in a fluid of mass density ρ_0 and bulk modulus b_0, as illustrated in Fig. 1(a). Active elements are connected to the waveguide wall in a periodic spacing $a/2$, positioned at x_n, and facing inward. These elements produce acoustic control velocities v_n, and are incorporated in the field equation as

$$\frac{1}{c^2}p_{tt}(x,t) = p_{xx}(x,t) + \rho_0\beta\sum_n \dot{v}_n(t)\delta(x-x_n), \qquad (1)$$

where $\delta(\cdot)$ is the Dirac delta function and β is the ratio between the active element area S_d and the waveguide cross section S_w. The actively controlled waveguide constitutes a hybrid continuous-discrete medium. The role of the inputs v_n is to increase the group velocity inside this medium, v_g, beyond the background speed of sound c. Motivated by control schemes for $\mathcal{PT}$-symmetric lattices [31,32], we define A and B sites alternating with the periodicity of a. Using feedback-control loops, the elements at these sites respectively induce local gain and loss defined by the parameter γ, as well as an additional coupling between each A-B pair, defined by the parameter η. We set the control inputs at these sites to

$$v_n^{A/B}(t) = \frac{\eta-1}{\rho_0 a}\int_0^t [p_n^{B/A}(t) - p_n^{A/B}(t)]\mathrm{d}t \pm \frac{\gamma}{z_0}p_n^{A/B}(t), \qquad (2)$$

where $p_n^{A/B}(t)$ is a compact form of $p(x_n^{A/B},t)$ and $z_0=\rho_0 c$ is the specific acoustic impedance. In closed loop, the pressure field in the waveguide is governed by

$$\begin{aligned}\frac{1}{c^2}p_{tt}(x,t) &= p_{xx}(x,t)\\ &\quad+\beta\sum_n\frac{\eta-1}{a}(p_n^B(t)-p_n^A(t))\delta(x-x_n^A)\\ &\quad+\beta\sum_n\frac{\eta-1}{a}(p_n^A(t)-p_n^B(t))\delta(x-x_n^B)\\ &\quad+\beta\frac{\gamma}{c}\sum_n\left[\dot{p}_n^A(t)\delta(x-x_n^A)-\dot{p}_n^B(t)\delta(x-x_n^B)\right]. \qquad (3)\end{aligned}$$

It is then required to derive a relation between γ and η so that $v_g > c$, but also that the stability of the system is preserved, i.e., that the waves propagate with nongrowing amplitudes. We thus consider an auxiliary model—an analogous mass-spring lattice, which is inherently discrete [Fig. 1(b)]—and derive the γ-η relation for this model first. Each lattice site has a single degree of freedom, the vertical displacement y. The masses M_0 and spring constants

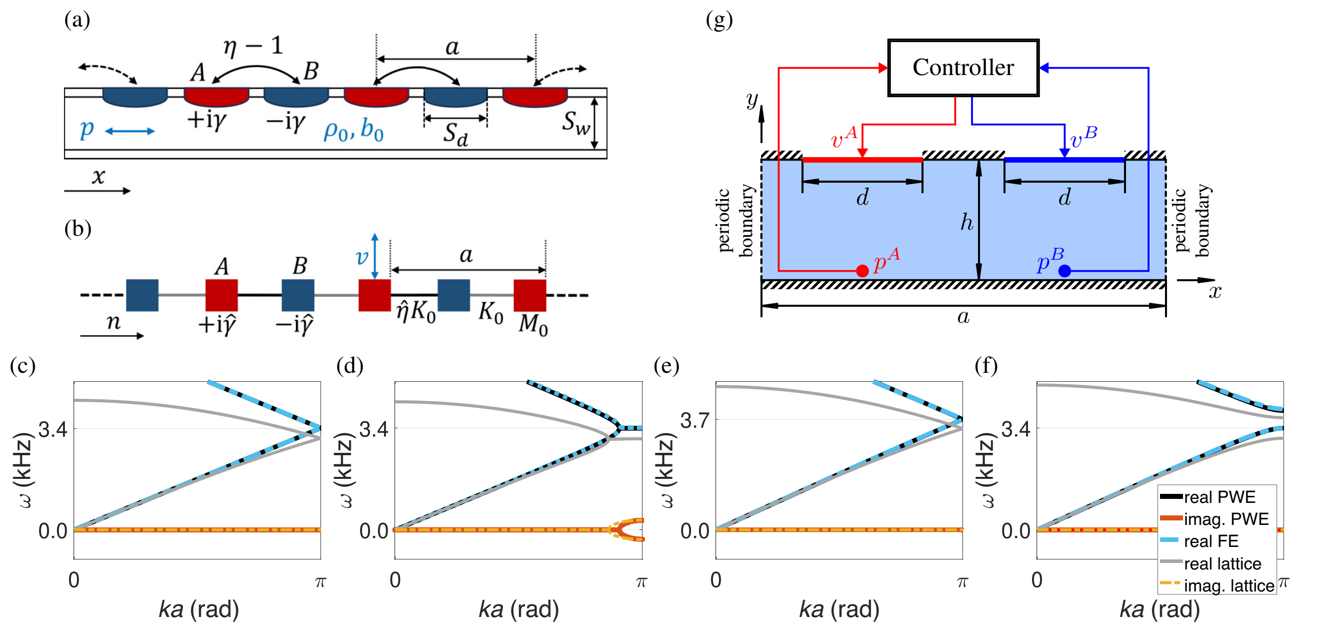

FIG. 1. The active acoustic metamaterial model and its spectral properties. (a) The schematics of the waveguide. (b) The schematics of the analogous lattice. (c)–(f) The frequency dispersion of the periodic system: (c) nominal stable, $\hat{\gamma} = \gamma = 0$, $\hat{\eta} = \eta = 1$; (d) unstable, $\hat{\gamma} = \gamma = 0.32$, $\hat{\eta} = \eta = 1$; (e) $\mathcal{PT}$-symmetry-restored stable, $\hat{\gamma} = 0.32$, $\gamma = 0.29$, $\hat{\eta} = 1.5$, $\eta = 2$; (f) gapped stable, $\hat{\gamma} = \gamma = 0$, $\hat{\eta} = 1.5$, $\eta = 2$. Gray and yellow, the lattice real and imaginary spectra according to Eq. (6); black and orange, the waveguide real and imaginary spectra calculated via plane wave expansion (PWE) according to Eqs. (C10) and (C11); cyan, the waveguide real spectrum calculated via finite-element (FE) analysis. $\beta = 1$ has been set in the waveguide. (g) A sketch of the FE model setup for numerically calculating the dispersion curves.

K_0 are analogous to the bulk modulus and mass density of the fluid as $M_0 \to aS_w/(2b_0)$ and $K_0 \to 2S_w/(\rho_0 a)$ and the site velocity $v = \dot{y}$ maps to the pressure p. Defining $\hat{\eta}K_0$ as a spring constant different to the nominal K_0 and $\mp \mathrm{i}\hat{\gamma} Z_0$ as an on-site viscous damper (antidamper) connected to ground, where $Z_0 = \sqrt{M_0 K_0}$ is the mechanical impedance, the dynamics of the nth A and B sites of the dimer lattice can be formulated as

$$\omega_0^{-2}\ddot{y}_n^{A/B} = y_{n\mp1}^{B/A} + \hat{\eta} y_n^{B/A} - (1+\hat{\eta}) y_n^{A/B} \pm \hat{\gamma}\omega_0^{-1}\dot{y}_n^{A/B}, \tag{4}$$

where $\omega_0 = \sqrt{K_0/M_0}$. The mapping between the γ and η couplings of the waveguide, and the $\hat{\gamma}$ and $\hat{\eta}$ couplings of the lattice, then take the form (see Appendix A)

$$\hat{\gamma} = \beta\gamma, \quad \hat{\eta} = \beta\tfrac{1}{2}(\eta - 1) + 1. \tag{5}$$

In order to derive the relation between $\hat{\gamma}$ and $\hat{\eta}$ for the group velocity increase, we insert the solution $[\,y_n^A\ y_n^B\,]^T = [\,\bar{y}^A\ \bar{y}^B\,]^T e^{\mathrm{i}(kna-\omega t)}$ in Eq. (4), where k is the wave number, and $\bar{y}^A, \bar{y}^B$ are the respective wave amplitudes. Defining the normalized frequency $\Omega = \omega/\omega_0$, we obtain the quadratic eigenvalue problem $\left(\Omega^2\mathbf{I} - \Omega \mathrm{i}\gamma\boldsymbol{\sigma}_z - \mathcal{H}_0 - (1+\eta)\mathbf{I}\right)[\,\bar{y}^A\ \bar{y}^B\,]^T = \mathbf{0}$, which can be augmented to $(\Omega\mathbf{I} - \mathcal{H})\,\bar{\mathbf{y}} = \mathbf{0}$, where $\bar{\mathbf{y}}$ is the augmented eigenvector that includes $\bar{y}^A, \bar{y}^B$, and two auxiliary states. The effective 4×4 Hamiltonian $\mathcal{H}$ is given by

$$\mathcal{H} = \begin{pmatrix} \mathbf{0} & \mathbf{I} \\ \mathcal{H}_0 + (1+\hat{\eta})\mathbf{I} & \mathrm{i}\hat{\gamma}\boldsymbol{\sigma}_z \end{pmatrix}, \quad \mathcal{H}_0 = \begin{pmatrix} 0 & f \\ f^\dagger & 0 \end{pmatrix}, \tag{6}$$

where $f = -\left[\hat{\eta} + e^{-\mathrm{i}ka}\right]$ and $\boldsymbol{\sigma}_z$ is the Pauli matrix. For $\hat{\gamma} > 0$, this Hamiltonian is non-Hermitian [1]. The solution of the eigenvalue problem in Eq. (6) gives the lattice dispersion relation and, consequently, the required relation between $\hat{\gamma}$ and $\hat{\eta}$ for dynamical stability [32]. This is illustrated in Figs. 1(c)–1(f). For the nominal lattice, i.e., for $\hat{\gamma} = 0$ and $\hat{\eta} = 1$, the spectrum is purely real, as expected [Fig. 1(c)], where the top band is idle (due to the lattice constant folding to $a/2$). When increasing $\hat{\gamma}$, the spectrum becomes complex valued around the band crossing point, turning it into an exceptional cut [4] [see Fig. 1(d)] (e.g., for $\hat{\gamma} = 0.32$). The time response at the nth node then takes the form $y_n(t) \propto e^{\omega_I t} e^{\mathrm{i}(kna - \omega_R t)}$, where ω_R and ω_I are the real and imaginary components of the frequency, respectively. The response thus grows unbounded, indicating the dynamical instability of the system. In particular, for

$$\hat{\gamma}_{pt} = \sqrt{2}\left(\sqrt{\hat{\eta}} - 1\right), \tag{7}$$

the lattice spectrum is restored to be purely real, as illustrated in Fig. 1(e) for $\hat{\eta} = 1.5$ and $\hat{\gamma} = 0.32$, while preserving the non-Hermiticity of the Hamiltonian in Eq. (6). This transition indicates the restoration of the $\mathcal{PT}$-symmetric phase [5]. For any $\hat{\gamma} < \hat{\gamma}_{pt}$, the spectrum remains real, albeit gapped, e.g., as shown in Fig. 1(f) for $\hat{\eta} = 1.5$ and $\hat{\gamma} = 0$, thus forming the lattice stability region in the $\hat{\gamma}$-$\hat{\eta}$ plane. Remarkably, the new crossing point of the dispersion curves for $\hat{\gamma} = \hat{\gamma}_{pt}$, which is an exceptional point, occurs at a higher frequency than for the nominal case, indicating an increase in group velocity. This increase is given by

$$v_g = v_0\sqrt{\tfrac{1}{\sqrt{2}}\hat{\gamma}_{pt} + 1}, \tag{8}$$

suggesting that it is possible to exceed the Hermitian group velocity v_0 and to guarantee dynamical stability (see Appendix B). Returning to the actual waveguide, we calculate the dispersion of Eq. (3) using the plane-wave-expansion (PWE) method [43], in which a series solution of traveling harmonic waves, $p(x,t) = \mathrm{e}^{\mathrm{i}\omega t}P(x)$, is assumed. Here, $P(x) = \sum_{m=-M}^{M} \mathrm{e}^{-\mathrm{i}(k+m)\mathbf{b}_1\cdot x\mathbf{d}_1}\overline{p}_m$, where $\mathbf{b}_1 = \frac{2\pi}{a}\hat{\mathbf{e}}_1$, and $\mathbf{d}_1 = a\hat{\mathbf{e}}_1$, respectively, span the momentum and the real spaces, $\overline{p}_m$ is the pressure field amplitude, and M is the approximation order (see Appendix C). Due to the continuity of the acoustic medium, there is an infinite number of bands, where M defines how many of these bands are plotted. The resulting spectrum is depicted on top of the lattice spectrum in Figs. 1(c)–1(f) in low frequencies for an air-filled waveguide. In these figures, the waveguide cross-section area is assumed to be equal to that of the active elements, i.e., $\beta = 1$, with a spacing of $a = 5$ cm, and $M = 4$.

In Fig. 1(c), we depict the spectrum of the uncontrolled waveguide. The crossing point of the main band with its folding, which occurs at $ka = \pi$, directly implies the slope of 343 m/s, which, as expected, equals c, the speed of sound in air. We then begin to increase γ while keeping $\eta = 1$. Similarly to the lattice system, we substitute $\gamma = 0.32$ and an imaginary spectrum appears, as depicted in Fig. 1(d). To eliminate the imaginary spectrum, we increase η as well. Since for $\hat{\gamma}_{pt} = 0.32$ the lattice balance relation in Eq. (7) reads $\hat{\eta} = 1.5$, the mapping to the waveguide in Eq. (5) implies $\eta = 2$.

However, as the analogy between discrete and continuous systems is valid only in the long-wavelength (low-frequency) regime, a discrepancy between the underlying spectra is observed at the vicinity of the crossing point $ka = \pi$ (given by $\omega = 2\sqrt{2}\sqrt{\sqrt{\hat{\eta}}}c/a$ in the lattice case). Therefore, to restore the $\mathcal{PT}$-symmetry in the waveguide for a given η, the value of γ stemming from Eqs. (5) and (7) needs to be slightly modified (the particular modification value depends on η; see Appendix A). For $\eta = 2$, the balance is then obtained for $\gamma_{pt} = 0.29$, as shown in Fig. 1(e). Decreasing γ below γ_{pt} keeps the spectrum real, albeit gapped, as in the lattice, as illustrated in Fig. 1(f) for $\eta = 2$ and $\gamma = 0$.

To confirm the results obtained via PWE, we calculate the frequency dispersion of the waveguide using finite-element (FE) analysis. As shown in Fig. 1(g), the domain is modeled as two-dimensional, representing a cross section of the waveguide with the main propagation axis x and the vertical axis y. The height of the waveguide h and the actuator length d are explicitly included in the model. The actuators are represented by velocity sources and point probes are used at the waveguide wall opposite to the actuators (similar to the experimental setup described in Sec. IV) to obtain the pressures p^A and p^B. Using these pressure values, the control law given in Eq. (2) is implemented to drive the velocity sources and create the required couplings. The ends of the waveguide section of length a, representing one unit cell, are terminated using periodic boundary conditions. All other boundaries are set to be sound hard. The dispersion curves have been calculated by computing the eigenvalues of the periodic system with different ka values. The FE results are depicted in Figs. 1(c)–1(f) on top of the PWE results, nearly coinciding with each other.

III. CONTROLLER DESIGN

We realize the control velocity sources using electroacoustic transducers, which replace the ideal actuators in Fig. 1(g). The control setup of each unit cell then consists of two speakers, which generate control velocities v_n^A and v_n^B, as well as two microphones, which measure the pressure signals p_n^A and p_n^B. Based on these measurements, the actuators create the γ and η couplings in real time. The structure of one actuator is detailed in Fig. 2(a). This is an electrodynamic loudspeaker within a closed cavity, which features a diaphragm mechanically driven by a voice coil, placed in a permanent magnetic field. At low frequencies, the loudspeaker can be approximated as a mass-spring-damper system and the diaphragm motion at small displacements can be described in the Laplace domain by [44,45] $Z_{mo}(s)v(s) = -S_d p(s) + Bli(s)$ and $u(s) = Z_{eb}(s)i(s) + Blv(s)$. Here, $Z_{mo}(s) = M_{ms}s + R_{ms} + 1/C_{ms}s$ and $Z_{eb}(s) = L_e s + R_e$ are, respectively, the open-circuit mechanical and the blocked electrical impedance of the loudspeaker, where M_{ms}, R_{ms}, and C_{mc} represent its moving mass, the mechanical damping, and the total mechanical compliance. S_d is the effective area of the diaphragm, with p being the total sound pressure acting on it, which includes both the incident and scattered pressure. v is the vibration velocity of the speaker diaphragm, i is the current in the voice coil, and u is the input voltage between the electrical terminals. Bl is the force factor of the speaker, where B is the magnetic field strength and l is the length of the voice coil wire in the magnetic field. R_e is the dc resistance and L_e is the self-inductance of the voice coil. To avoid the impact of the coil inductance L_e on the system stability, we have designed our loudspeakers to be

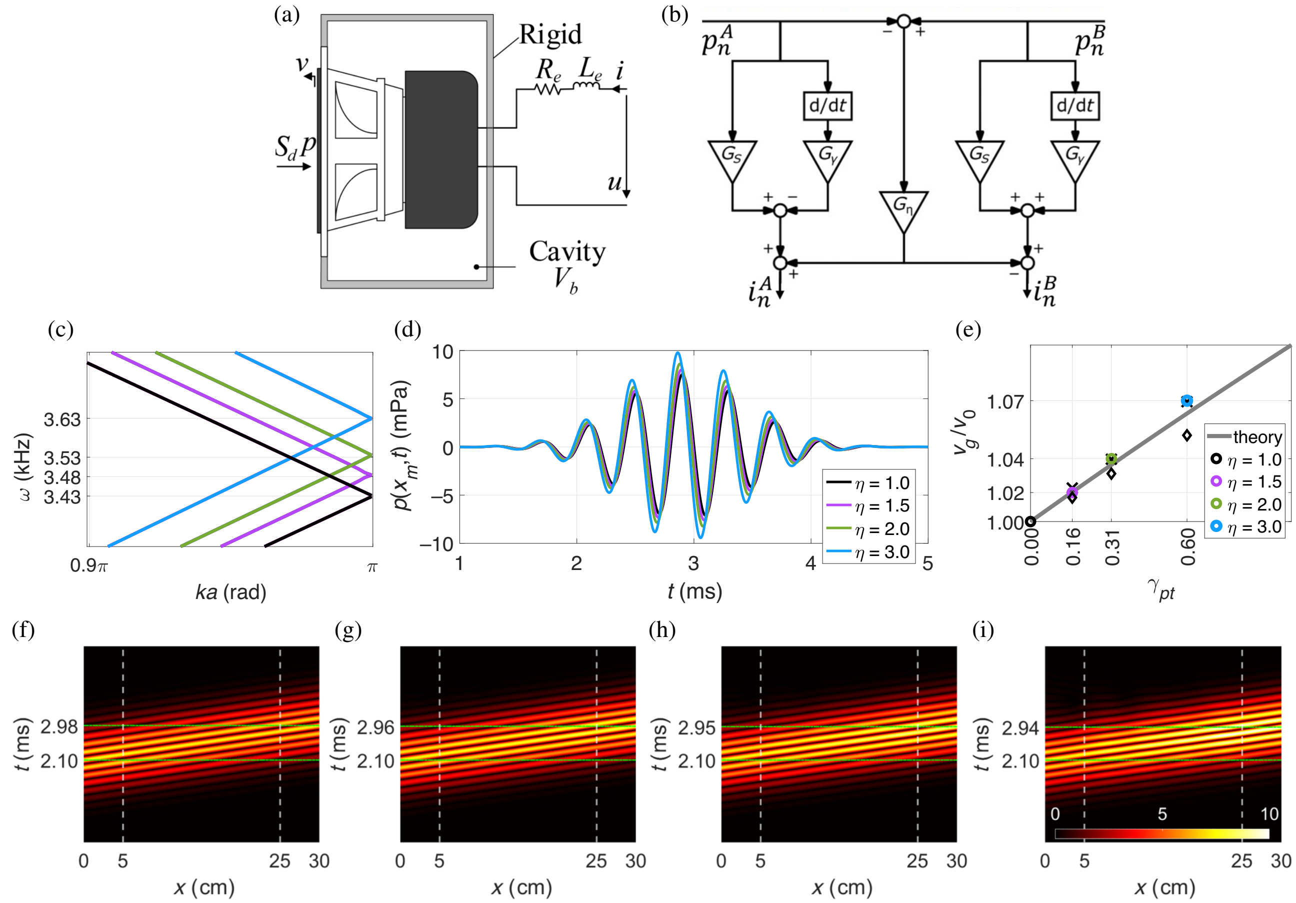

FIG. 2. Waveguide realization in a feedback-control setup using current-driven electroacoustic transducers. (a) A schematic of the electrodynamic speaker. (b) The controller structure. (c) The waveguide dispersion relation obtained from PWE for $a = 5$ cm and $\beta = 0.32$, featuring the uncontrolled case $\gamma = 0, \eta = 1$ (black) and the controlled cases $\gamma = 0.16, \eta = 1.5$ (purple), $\gamma = 0.31, \eta = 2$ (green), and $\gamma = 0.60, \eta = 3$ (blue). (d) Time-domain responses to a Gaussian wave packet centered at $\omega = 2.5$ kHz, calculated via FE. (e) The normalized group velocities obtained from the time-domain simulations (circles) and from the corresponding dispersion plots in (c) (black diamonds, $\omega = 2.5$ kHz$-$; black crosses, $\omega = 0$ kHz$-$), plotted on top of the theoretical expression given in Eq. (8) via Eq. (5) (gray). (f)–(i) The corresponding full-wave FE simulations, showing the absolute value of the pressure in mPa for (f) $\eta = 1$, (g) $\eta = 1.5$, (h) $\eta = 2$, and (i) $\eta = 3$, respectively, depicting decreasing wave-packet arrival times with the same initial time for increasing η values (both times are indicated by horizontal dashed green lines). The vertical dashed white lines indicate the beginning and the end of the active part of the waveguide.

driven by current sources. We set the control law in each unit cell to

$$i_n^{A/B}(s) = (G_S \pm sG_\gamma)p_n^{A/B}(s) + G_\eta\left[p_n^{B/A}(s) - p_n^{A/B}(s)\right], \tag{9}$$

which results in the acoustic velocity commands

$$v_n^{A/B}(s) = \frac{-S_d + Bl(G_S \pm sG_\gamma)}{Z_{mo}(s)}p_n^{A/B}(s) + \frac{BlG_\eta}{Z_{mo}(s)}\left[p_n^{B/A}(s) - p_n^{A/B}(s)\right]. \tag{10}$$

Comparing Eq. (10) with Eq. (2) and assuming that $Z_{mo}(s) \approx M_{ms}s$ in our working frequency range (above the mechanical resonance frequency of the loudspeakers), the controller gains take the form

$$G_S = \frac{S_d}{Bl},\ G_\gamma = \frac{\gamma M_{ms}}{Blz_0},\ G_\eta = \frac{(\eta-1)M_{ms}}{\rho_0 aBl}. \tag{11}$$

The structure of the control law in Eq. (9) with Eq. (11) is schematically illustrated in Fig. 2(b). The gain G_S is responsible for the cancellation of the internal physical feedback of the loudspeaker, whereas G_γ and G_η create the γ and the η couplings, respectively. We then demonstrate the performance of our controlled waveguide using a numerical experiment with $\beta = 0.32$ (to be aligned with the actual experiment; see Sec. IV). We calculate the controller gains for the cases $\eta = 1.5$, 2, and 3. For these values of η, we have $\hat{\eta} = 1.08$, 1.16, and 1.32 by Eq. (5), then $\hat{\gamma} = 0.06$, 0.11, and 0.21 by Eq. (7), and $\gamma = 0.17$, 0.34, and 0.66 back by Eq. (5). Using final modification, the corresponding values of $\gamma = 0.16$, 0.31, and 0.60 are obtained. The dispersion relations of the resulting closed loops, calculated at low frequencies by PWE, are depicted in Fig. 2(c), on top of the uncontrolled case $\eta = 1$, $\gamma = 0$. The slope of the spectrum increases with γ, indicating an increase in group velocity. However, due to $\beta < 1$, the achieved slope, and thus the v_g increase for the same η, is less than in Fig. 1(e).

A waveguide controlled by the feedback system in Figs. 2(a) and 2(b) for the above combinations of γ and η has then been simulated in the time domain using FE. The FE model consisted of a waveguide with four unit cells and was terminated on both ends by absorbing boundary conditions. A low-pass filter was applied to the current control signals to minimize the generation of higher-order nonplane waves in the waveguide. The responses to a Gaussian wave packet are given in Fig. 2(d). The group velocities calculated from these responses are depicted in Fig. 2(e) on top of the theoretical expression in Eq. (8) [via the mapping in Eq. (5)], and those calculated from the dispersion curves in Fig. 2(c), both for the central frequency of the wave packet and for zero (the dispersion slope is monotonically decreasing with the frequency). The group velocities obtained from the time-domain simulations are closer to the small frequency values. The corresponding full-wave FE simulations, showing the absolute value of the pressure in mPa for $\eta = 1$, 1.5, 2, and 3, are shown in Figs. 2(f)–2(i), respectively, depicting decreasing wave-packet arrival times with the same initial time for increasing η values.

IV. EXPERIMENTAL DEMONSTRATION

To confirm the group velocity increase, an active metastructure has been fabricated, as shown in the schematic of Fig. 3(a) and the photograph of Fig. 3(b). The sound source is positioned at the left end of the waveguide, whereas the right end contains glass wool for sound-wave absorption, sealed by a 4-mm-thick resin block. The waveguide has a uniform wall thickness of 4 mm, produced via three-dimensional printing using a resin material with a density of 1180 kg/m^3. The waveguide has a length of 1 m and a square cross section with dimensions of 15×15 mm^2, corresponding to a cutoff frequency for the plane-wave mode of 11 467 Hz. The active metamaterial, 20 cm in total length, consists of four unit cells (eight active sites) positioned in the center of the waveguide.

Each unit cell, measuring $a = 5$ cm, contains two identical loudspeakers on the top and two identical microphones on the bottom. Two additional microphones, Mic1 and Mic4, are symmetrically positioned on the left and right sides of the active metamaterial, spaced 60 cm apart, to monitor the velocity of acoustic wave propagation. A controller corresponding to Fig. 2(b) has been designed to regulate the output of the control sources A and B. This has been realized using voltage-controlled current sources (VCCS), which convert a voltage signal into a proportional current signal with unity gain to drive the loudspeakers, as detailed in Appendix D. The output voltage signals of the controller, u_n^A and u_n^B, are therefore converted into current signals as $i_n^{A/B} = G u_n^{A/B}$, where $G = 1$ A/V.

To ensure consistency between the loudspeakers and microphones, careful selections and calibrations have been performed. The Thiele & Small parameters of the loudspeakers have been measured using the Klippel electroacoustic test system. The following average parameters have been obtained: diaphragm mass $M_{ms} = 0.0689$ g, force factor $Bl = 0.606$ N/A, and effective diaphragm area $S_d = 72$ mm^2, leading to $\beta = 0.32$, and resonance frequency 900 Hz. Electret condenser microphones have been used as the pressure sensors. The microphone signals have been amplified to ensure a sensitivity of $S_0 =$ 400 mV/Pa. The controller has been designed using analog circuitry and fabricated using a printed circuit board (see Appendix D). Potentiometers have been used to adjust G_γ and G_η to achieve the desired different values of γ and η according to Eq. (11), divided by S_0. An NI acquisition card with a sampling rate of $f_s = 200$ kHz has been used to record the microphone signals from Mic1 and Mic4.

The signal supplied to the sound source was a Gaussian pulse modulated by a 2500-Hz sine wave. Three sets of measurements have been conducted with $\eta = 1$, 1.5, and 2, respectively, and the corresponding γ has been calculated from Eqs. (5) and (7) to be 0, 0.16, and 0.31. The measurement results are presented in Fig. 3(c), with a close-up in Fig. 3(d). These results compare the pulse waveform over time for the Hermitian case $\gamma = 0$, $\eta = 1$ with the non-Hermitian cases $\eta = 1.5$ and $\eta = 2$. For higher η, we have observed instability in the measured responses. Setting the peak time of the pulse recorded by microphone Mic1 as 0, the peak arrival times at microphone Mic4 are advanced by $\delta_t = 0.01$ ms and $\delta_t = 0.02$ ms for $\eta = 1.5$ and $\eta = 2$, respectively. This confirms that the acoustic wave speed increased.

The actual group velocity v_g of the sound wave in the metamaterial can be determined by the equation $l/c - l/v_g = \delta_t$, where $l = 20$ cm is the total length of the active part. The baseline speed c has been obtained as 333 m/s by measurement at a room temperature of 20 °C, i.e., $c = s/t_0$, where $s = 60$ cm denotes the distance between microphones Mic1 and Mic4, and $t_0 = 1.8$ ms is the time difference between the pulse arriving at Mic4 and Mic1 in the Hermitian case. Therefore, for the non-Hermitian cases $\eta = 1.5$ and $\eta = 2$, the sound-wave velocities in the active metamaterial read 339 m/s and 345 m/s, respectively. In Fig. 3(e), we compare experimental and theoretical results [the time domain FE simulations of Fig. 2(d)]. The discrepancy between the theoretical and

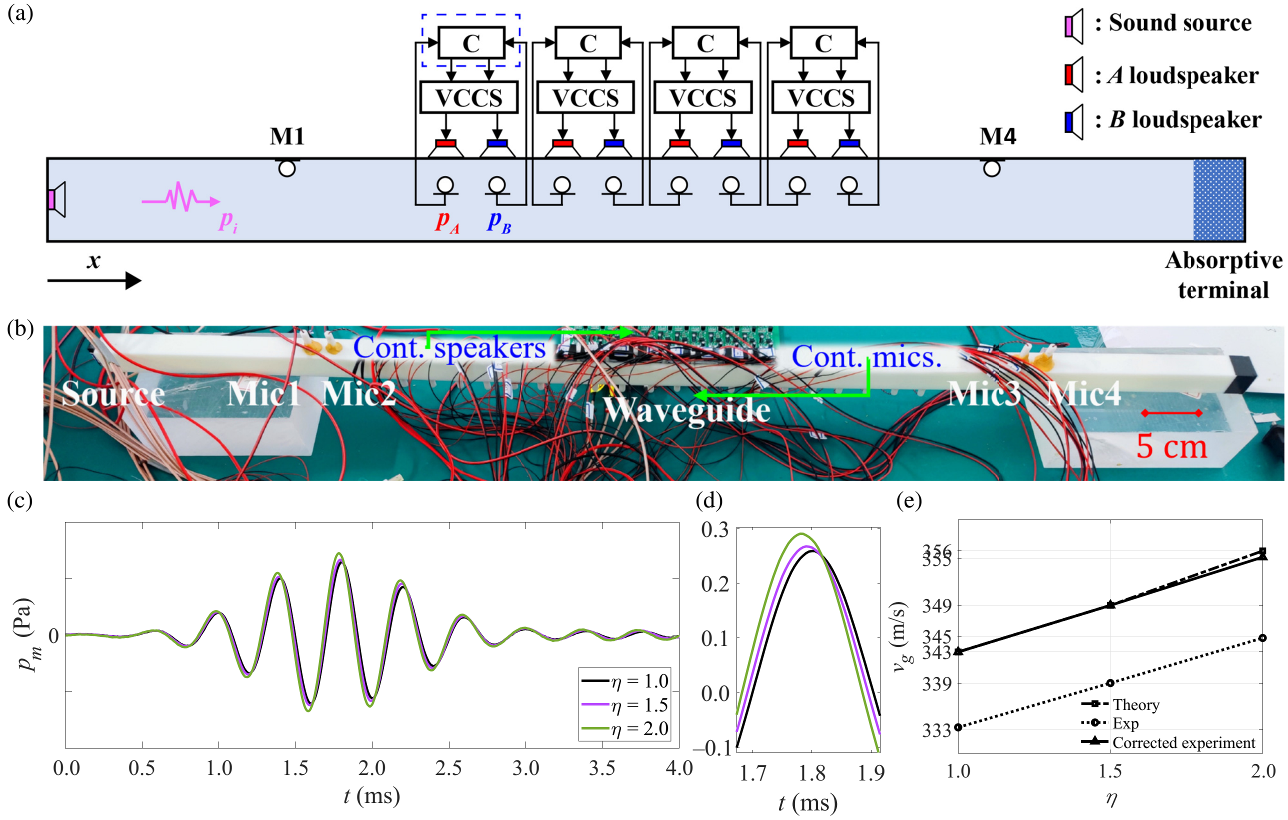

FIG. 3. An experimental demonstration of accelerated wave-packet propagation. (a) A schematic of the experimental setup. (b) A photograph of the waveguide, comprising eight active sites. (c) The measured waveform at microphone Mic4 relative to microphone Mic1 as a function of time for $\eta = 1$ (black), $\eta = 1.5$ (purple), and $\eta = 2$ (green). (d) A close-up of the measured waveform in (c). (e) A comparison of the calculated group velocities with the measured results: dashed, the theoretical values obtained from Eq. (8) via Eq. (5); dotted, the measured values; solid, the measured values adjusted to the Hermitian velocity of 343 m/s.

experimental results is attributed to the measured baseline sound velocity $c = 333$ m/s being lower than the theoretically expected value of 343 m/s at room temperature. This deviation primarily stems from measurement uncertainties (e.g., misalignment between the acoustic and physical centers of microphones Mic1 and Mic4, manufacturing and assembly tolerances for the waveguide, and temporal resolution of the sampled pressure signals) and thermoviscous boundary layer effects slowing down the sound velocity in the waveguide [46]. Correcting to the theoretical room-temperature sound speed $c = 343$ m/s, the experimental results become $v_g = 349$ m/s for $\eta = 1.5$ and $v_g = 355$ m/s for $\eta = 2$. The corrected values, shown as the solid line in Fig. 3(e), align closely with the theoretical results.

V. DISCUSSION AND CONCLUSIONS

In this work, we have suggested a mechanism to enhance the sound velocity in a waveguide by lifting up the crossing point—and thus the slope—of the underlying dispersion relation without any change to the medium properties or the waveguide geometry. Rather, the slope increase has been achieved by inducing non-Hermiticity through active control elements seamlessly sealed in the waveguide wall. The idea has been based on an equivalent lattice model [Fig. 1(b)] and then mapped to the waveguide system [Fig. 1(a)].

The balance between the control parameters—the local gain-loss couplings γ and the nonlocal couplings η that we have derived for the waveguide system via the analogous lattice system [see Eqs. (5) and (7)]—addresses the challenge of merging a spatially discrete coupling pattern into the continuous waveguide medium. The final modification of the balance due to the analogy being valid only in the long-wavelength regime, has been minor for small η, but still required. As a result, a real spectrum has been restored in the low-frequency range and the desired faster-than-sound dynamics have been achieved, manifested by the group velocity growth being proportional to the square root of γ. In practice, there will be a limitation to the achievable group velocity, as one cannot generate either an infinite γ or an infinite η [47].

The FE and PWE simulations have suggested that, theoretically, the waveguide system is stable for the achieved group velocities. In our experiment, we have managed to maintain stable propagation for a velocity increase of up to 355 m/s from the nominal 343 m/s. We anticipate that this limit can be further pushed by optimizations of the control setup and algorithm. Our active coupling approach is advantageous in applications that forbid waveguide cross-section blocking and/or require long-range coupling between multiple active cells. Compared to purely passive systems, the active approach enables the modulation profile to be easily reconfigured to more complex interactions, which could lead to new wave properties and wave-guiding capabilities.

ACKNOWLEDGMENTS

K. W., H. Z., and J. L. have been supported by the National Natural Science Foundation of China (Grant No. 12274221). F.L. has been partially supported by the United Kingdom (UK) Engineering and Physical Sciences Research Council (EPSRC) through the third funding call by the UK Acoustics Network Plus EP/V007866/1. C.S. acknowledges support from the National Science Foundation under Grant No. ECCS-2337069. L.S. was partially supported by the Israel Science Foundation (Grants No. 2177/23 and No. 2876/23).

DATA AVAILABILITY

The data that support the findings of this paper are not publicly available upon publication because it is not technically feasible and/or the cost of preparing, depositing, and hosting the data would be prohibitive within the terms of this research project. The data are available from the authors upon reasonable request.

APPENDIX A: MAPPING BETWEEN THE LATTICE AND THE WAVEGUIDE

Here, we provide derivation details of the mapping in Eq. (5). The lattice equation in Eq. (4) is the result of the inhomogeneous mass-spring system

$$\begin{cases} M_0\ddot{y}_n^A = K_0\left(y_n^B - 2y_n^A + y_{n-1}^B\right) + F_n^A, \\ M_0\ddot{y}_n^B = K_0\left(y_{n+1}^A - 2y_n^B + y_n^A\right) + F_n^B, \end{cases} \tag{A1}$$

being controlled in closed loop by the input forces

$$\begin{cases} F_n^A = K_0\left(\hat{\eta}-1\right)\left[y_n^B - y_n^A\right] + \hat{\gamma}\sqrt{K_0M_0}\dot{y}_n^A, \\ F_n^B = K_0\left(\hat{\eta}-1\right)\left[y_n^A - y_n^B\right] - \hat{\gamma}\sqrt{K_0M_0}\dot{y}_n^B. \end{cases} \tag{A2}$$

Since $M_0\ddot{y}_n = K_0\left(y_{n+1} - 2y_n + y_{n-1}\right) + F_n$, a general forced lattice equation maps to the inhomogeneous acoustic waveguide given in Eq. (1), and the lattice site displacement y maps to the integral of pressure p, while the lattice control inputs F in Eq. (A2) are mapped to the acoustic

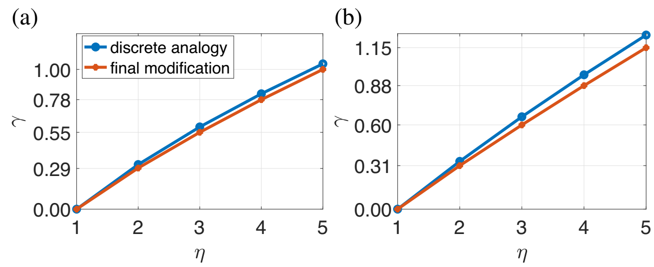

FIG. 4. The $\mathcal{PT}$-symmetry $\gamma - \eta$ balance in the waveguide: (a) $\beta = 1$; (b) $\beta = 0.32$. Blue, the γ value implied by Eqs. (5) and (7); orange, the actual γ value obtained by final modification.

inputs as βv, i.e.,

$$\begin{cases} v_n^A = \dfrac{2(\hat{\eta}-1)}{\beta\rho_0 a}\displaystyle\int_0^t\left[p_n^B - p_n^A\right]\mathrm{d}t + \dfrac{\hat{\gamma}}{\beta z_0}p_n^A, \\ v_n^B = \dfrac{2(\hat{\eta}-1)}{\beta\rho_0 a}\displaystyle\int_0^t\left[p_n^A - p_n^B\right]\mathrm{d}t - \dfrac{\hat{\gamma}}{\beta z_0}p_n^B. \end{cases} \tag{A3}$$

Comparing Eq. (A3) with the actual acoustic inputs in Eq. (2), the mapping of Eq. (5) is straightforwardly obtained. The final modification of γ for a fixed η, which is required due to the discrepancy between the continuous and the equivalent discrete model at the crossing point, is illustrated in Fig. 4. Both for $\beta = 1$ and $\beta = 0.32$, the actual value of γ that is required to restore $\mathcal{PT}$-symmetry in the waveguide is slightly smaller than the value that stems from Eqs. (5) and (7).

APPENDIX B: GROUP VELOCITY CONTROL IN THE LATTICE MODEL

The analogous lattice model in Fig. 1(b) is represented by the augmented eigenvalue problem in Eq. (6), which reads

$$\Omega^4 - \left(2(1+\hat{\eta}) - \hat{\gamma}^2\right)\Omega^2 + (1+\hat{\eta})^2 - ff^\dagger = 0. \tag{B1}$$

Its solution is given by

$$\Omega^2 = \tfrac{1}{2}\left(2(1+\hat{\eta}) - \hat{\gamma}^2\right) \pm \tfrac{1}{2}\sqrt{\delta}, \tag{B2}$$

with $\delta = \left(2(1+\hat{\eta}) - \hat{\gamma}^2\right)^2 - 4\left((1+\hat{\eta})^2 - ff^\dagger\right)$. The requirements for a real spectrum (with a minimum at $\cos ka = -1$) give the $\mathcal{PT}$-symmetry condition $\hat{\gamma} \le \hat{\gamma}_{pt}$ of Eq. (7) via Eq. (5). We then obtain $(1+\hat{\eta})^2 - ff^\dagger = 2\hat{\eta}(1-\cos ka)$ and $\delta = 8\hat{\eta}(1+\cos ka)$, and the dispersion relation is obtained from Eq. (B2) as

$$\Omega = \sqrt{\sqrt{2}\hat{\gamma}_{pt} + 2}\cdot\sqrt{1 \pm \sqrt{\tfrac{1}{2}\left(1+\cos ka\right)}}. \tag{B3}$$

In the Hermitian case, the lattice constant is $a/2$. We then use the identity $\cos ka = \cos^2 ka/2 - \sin^2 ka/2$, which implies that $\sqrt{\frac{1}{2}(1+\cos ka)}$ is equal to $\cos(ka/2)$, with the positive branch chosen for $k \in [0, \pi/a]$ and the negative branch for $k \in (\pi/a, 2\pi/a]$. We then rewrite Ω in Eq. (B3) as a function of the Hermitian frequency spectrum, as

$$\Omega = \sqrt{\tfrac{1}{\sqrt{2}}\hat{\gamma}+1}\,\Omega_H, \quad \Omega_H = \sqrt{2}\sqrt{1-\cos\tfrac{ka}{2}}. \tag{B4}$$

The group velocity (normalized by ω_0) thus becomes

$$v_g = \frac{\partial \Omega}{\partial k} = \sqrt{\tfrac{1}{\sqrt{2}}\hat{\gamma}+1}\,\frac{\partial \Omega_H}{\partial k} = \sqrt{\tfrac{1}{\sqrt{2}}\hat{\gamma}+1}\,v_0, \tag{B5}$$

where v_0 is the Hermitian group velocity, given by

$$v_0 = \frac{a\sin\frac{ka}{2}}{2\sqrt{2}\sqrt{1-\cos\frac{ka}{2}}}. \tag{B6}$$

APPENDIX C: THE PLANE-WAVE-EXPANSION DERIVATION

We substitute the proposed solution $p(x,t) = \mathrm{e}^{\mathrm{i}\omega t}P(x)$, with $P(x) = \sum_{m=-M}^{M} \mathrm{e}^{-\mathrm{i}(k+m)\mathbf{b}_1\cdot x\mathbf{d}_1}\overline{p}_m$, $\mathbf{b}_1 = \frac{2\pi}{a}\hat{\mathbf{e}}_1$ and $\mathbf{d}_1 = a\hat{\mathbf{e}}_1$, into the nth unit cell of Eq. (3). Using a general formulation $\mathbf{r} = x\mathbf{d}_1$, $\mathbf{k} = k\mathbf{b}_1$, and $\mathbf{G} = m\mathbf{b}_1$, and transforming p_{tt}, p_t to the frequency domain as $-\omega^2 p, \mathrm{i}\omega p$, reads

$$\begin{aligned}
\frac{\omega^2}{c^2}\sum_{m=-M}^{M} e^{-\mathrm{i}(\mathbf{k}+\mathbf{G})\cdot\mathbf{r}}\overline{p}_m &= \sum_{m=-M}^{M} |\mathbf{k}+\mathbf{G}|^2 e^{-\mathrm{i}(\mathbf{k}+\mathbf{G})\cdot\mathbf{r}}\overline{p}_m \\
&- \beta\sum_{m=-M}^{M}\Bigg[\frac{\eta-1}{a}\left(e^{-\mathrm{i}(\mathbf{k}+\mathbf{G})\cdot\mathbf{R}_B} - e^{-\mathrm{i}(\mathbf{k}+\mathbf{G})\cdot\mathbf{R}_A}\right) \\
&- \frac{\gamma}{c}\mathrm{i}\omega e^{-\mathrm{i}(\mathbf{k}+\mathbf{G})\cdot\mathbf{R}_A}\Bigg]\delta(\mathbf{r}-\mathbf{R}_A)\overline{p}_m \\
&- \beta\sum_{m=-M}^{M}\Bigg[\frac{\eta-1}{a}\left(e^{-\mathrm{i}(\mathbf{k}+\mathbf{G})\cdot\mathbf{R}_A} - e^{-\mathrm{i}(\mathbf{k}+\mathbf{G})\cdot\mathbf{R}_B}\right) \\
&+ \frac{\gamma}{c}\mathrm{i}\omega e^{-\mathrm{i}(\mathbf{k}+\mathbf{G})\cdot\mathbf{R}_B}\Bigg]\delta(\mathbf{r}-\mathbf{R}_B)\overline{p}_m,
\end{aligned} \tag{C1}$$

where $\mathbf{R}_A = -\frac{1}{4}\mathbf{d}_1$ and $\mathbf{R}_B = \frac{1}{4}\mathbf{d}_1$ are the actuator locations measured from the center of the unit cell. Multiplying Eq. (C1) by $e^{\mathrm{i}(\mathbf{k}+\widehat{\mathbf{G}})\cdot\mathbf{r}}$, where $\widehat{\mathbf{G}} = \widehat{m}\mathbf{b}_1$, gives

$$\begin{aligned}
\frac{\omega^2}{c^2}\sum_{m=-M}^{M} e^{-\mathrm{i}(\mathbf{G}-\widehat{\mathbf{G}})\cdot\mathbf{r}}\overline{p}_m &= \sum_{m=-M}^{M} |\mathbf{k}+\mathbf{G}|^2 e^{-\mathrm{i}(\mathbf{G}-\widehat{\mathbf{G}})\cdot\mathbf{r}}\overline{p}_m \\
&- \beta\sum_{m=-M}^{M} e^{\mathrm{i}(\mathbf{k}+\widehat{\mathbf{G}})\cdot\mathbf{r}}\Bigg(\frac{\eta-1}{a}\left[e^{-\mathrm{i}(\mathbf{k}+\mathbf{G})\cdot\mathbf{R}_B} - e^{-\mathrm{i}(\mathbf{k}+\mathbf{G})\cdot\mathbf{R}_A}\right] \\
&- \frac{\gamma}{c}\mathrm{i}\omega e^{-\mathrm{i}(\mathbf{k}+\mathbf{G})\cdot\mathbf{R}_A}\Bigg)\delta(\mathbf{r}-\mathbf{R}_A)\overline{p}_m \\
&- \beta\sum_{m=-M}^{M} e^{\mathrm{i}(\mathbf{k}+\widehat{\mathbf{G}})\cdot\mathbf{r}}\Bigg(\frac{\eta-1}{a}\left[e^{-\mathrm{i}(\mathbf{k}+\mathbf{G})\cdot\mathbf{R}_A} - e^{-\mathrm{i}(\mathbf{k}+\mathbf{G})\cdot\mathbf{R}_B}\right] \\
&+ \frac{\gamma}{c}\mathrm{i}\omega e^{-\mathrm{i}(\mathbf{k}+\mathbf{G})\cdot\mathbf{R}_B}\Bigg)\delta(\mathbf{r}-\mathbf{R}_B)\overline{p}_m.
\end{aligned} \tag{C2}$$

Due to the orthogonality of the Fourier series, we have

$$\int_{A_c} e^{-\mathrm{i}(\mathbf{G}-\widehat{\mathbf{G}})\cdot\mathbf{r}}\mathrm{d}A_c = \begin{cases} A_c, & \mathbf{G} = \widehat{\mathbf{G}}, \\ 0, & \mathbf{G} \neq \widehat{\mathbf{G}}. \end{cases} \tag{C3}$$

Also, we have

$$\int_{A_c} f(\mathbf{r})\delta(\mathbf{r}-\mathbf{R}_\alpha)\mathrm{d}A_c = f(\mathbf{R}_\alpha), \tag{C4}$$

where $A_c = a$ is the unit cell length and the lattice constant. Integrating Eq. (C2) over a unit cell and solving for all $\widehat{m}$ in the range $-M, \ldots, M$, then gives

$$\begin{aligned}
\frac{\omega^2}{c^2}a\mathbf{I}_N\overline{\mathbf{p}} = \mathbf{W}a\overline{\mathbf{p}} &- \beta\sum_{m=-M}^{M}\Bigg(\frac{\eta-1}{a}e^{\mathrm{i}\mathbf{k}\cdot(\mathbf{R}_A-\mathbf{R}_B)}e^{\mathrm{i}\widehat{\mathbf{G}}\cdot\mathbf{R}_A}e^{-\mathrm{i}\mathbf{G}\cdot\mathbf{R}_B}\overline{p}_m \\
&+ \left[\frac{\eta-1}{a} + \frac{\gamma}{c}\mathrm{i}\omega\right]e^{-\mathrm{i}(\mathbf{G}-\widehat{\mathbf{G}})\cdot\mathbf{R}_A}\overline{p}_m\Bigg) \\
&- \beta\sum_{m=-M}^{M}\Bigg(\frac{\eta-1}{a}e^{\mathrm{i}\mathbf{k}\cdot(\mathbf{R}_B-\mathbf{R}_A)}e^{\mathrm{i}\widehat{\mathbf{G}}\cdot\mathbf{R}_B}e^{-\mathrm{i}\mathbf{G}\cdot\mathbf{R}_A}\overline{p}_m \\
&+ \left[\frac{\eta-1}{a} - \frac{\gamma}{c}\mathrm{i}\omega\right]e^{-\mathrm{i}(\mathbf{G}-\widehat{\mathbf{G}})\cdot\mathbf{R}_B}\overline{p}_m\Bigg),
\end{aligned} \tag{C5}$$

where $N = 2M+1$ is the total number of terms in the series,

$$\mathbf{W} = \begin{pmatrix} |\mathbf{k}+\widehat{\mathbf{G}}_1|^2 & & \\ & \cdots & \\ & & |\mathbf{k}+\widehat{\mathbf{G}}_N|^2 \end{pmatrix}, \tag{C6}$$

$\overline{\mathbf{p}}$ is the eigenvector of length N, $\mathbf{G}\cdot\mathbf{R}_A = -\frac{\pi}{2}m$, and $\mathbf{G}\cdot\mathbf{R}_B = \frac{\pi}{2}m$. Using matrix formulation, we define

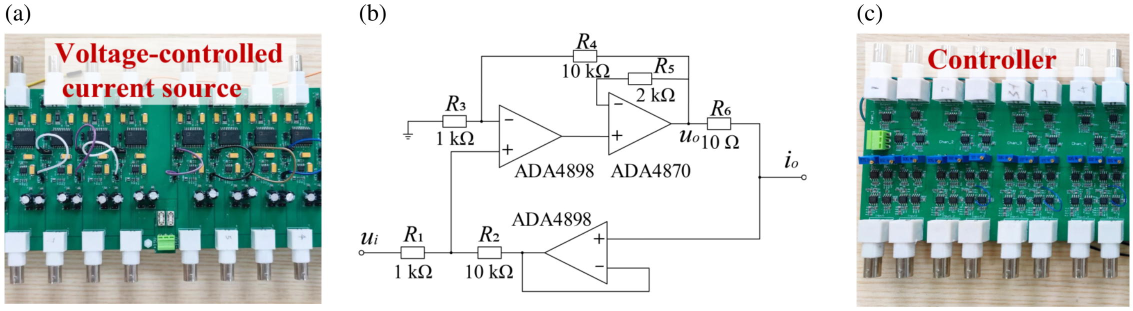

FIG. 5. (a),(b) Realization of the controller of Fig. 2(b): (a) a photograph and (b) the circuitry of the voltage-controlled current sources (VCCS). (c) A photograph of the controller.

$\sum_{m=-M}^{M} e^{\mathrm{i}\widehat{\mathbf{G}}\cdot\mathbf{R}_{\widehat{j}}} e^{-\mathrm{i}\mathbf{G}\cdot\mathbf{R}_j} \overline{p}_m = \mathbf{E}_{\widehat{j}j}\overline{\mathbf{p}}$, where

$$\mathbf{E}_{\widehat{j}j} = e^{\mathrm{i}\begin{bmatrix}\mathbf{G}_1 & \mathbf{G}_2 & \cdots & \mathbf{G}_N\end{bmatrix}'\cdot\mathbf{R}_{\widehat{j}}} \cdot e^{-\mathrm{i}\mathbf{R}_j\cdot\begin{bmatrix}\mathbf{G}_1 & \mathbf{G}_2 & \cdots & \mathbf{G}_N\end{bmatrix}}, \tag{C7}$$

and j and $\widehat{j}$ take the according values of A and B. Equation (C5) then takes the form of the polynomial eigenvalue problem,

$$\left(\mathbf{q}_2\omega^2 + \mathbf{q}_1\omega + \mathbf{q}_0\right)\overline{\mathbf{p}} = 0, \tag{C8}$$

where

$$\begin{aligned}\mathbf{q}_2 &= \frac{a}{c^2}\mathbf{I}_N,\\ \mathbf{q}_1 &= -\beta\frac{\gamma}{c}\mathrm{i}\left(\mathbf{E}_{\widehat{A}A} - \mathbf{E}_{\widehat{B}B}\right),\\ \mathbf{q}_0 &= -a\mathbf{W} + \beta\frac{\eta-1}{a}\left(e^{\mathrm{i}\mathbf{k}\cdot(\mathbf{R}_A-\mathbf{R}_B)}\mathbf{E}_{\widehat{A}B} + \mathbf{E}_{\widehat{A}A}\right.\\ &\quad\left.+e^{\mathrm{i}\mathbf{k}\cdot(\mathbf{R}_B-\mathbf{R}_A)}\mathbf{E}_{\widehat{B}A} - \mathbf{E}_{\widehat{B}B}\right).\end{aligned} \tag{C9}$$

We then rewrite Eqs. (C8) and (C9) in a companion form to obtain an augmented linear eigenvalue problem,

$$\omega\mathbf{P}\mathbf{v} = \mathbf{Q}\mathbf{v}, \tag{C10}$$

where $\mathbf{v}$ is the augmented eigenvector of length $2N$ and

$$\mathbf{P} = \begin{pmatrix}\mathbf{I} & 0\\ 0 & \mathbf{q}_2\end{pmatrix}, \quad \mathbf{Q} = \begin{pmatrix}0 & \mathbf{I}\\ -\mathbf{q}_0 & -\mathbf{q}_1\end{pmatrix}. \tag{C11}$$

The solution of Eqs. (C10) and (C11) gives the black and orange dispersion curves in Figs. 1(c)–1(f).

APPENDIX D: THE CONTROLLER STRUCTURE

The VCCS employed in our experiment, photographed in Fig. 5(a), has been designed using an improved Howland current-pump circuit [48]. It integrates the high output of operational amplifier ADA4870 with the fast response of operational amplifier ADA4898. The relation between the output current i_o and the input voltage u_i then becomes

$$i_o = \frac{R_2}{R_1R_6}u_i + \frac{R_2R_3 - R_1R_4}{R_1R_6(R_3+R_4)}u_o,$$

as illustrated in Fig. 5(b). Substituting the resistor values from Fig. 5(b) yields the output current $i_o = Gu_i$, where $G = 1$ A/V. The circuit performance has been verified via MULTISIM simulations. The resulting controller is photographed in Fig. 5(c).

[1] Y. Ashida, Z. Gong, and M. Ueda, Non-Hermitian physics, Adv. Phys. **69**, 249 (2020).
[2] K. Ding, C. Fang, and G. Ma, Non-Hermitian topology and exceptional-point geometries, Nat. Rev. Phys. **4**, 745 (2022).
[3] R. El-Ganainy, K. G. Makris, M. Khajavikhan, Z. H. Musslimani, S. Rotter, and D. N. Christodoulides, Non-Hermitian physics and PT symmetry, Nat. Phys. **14**, 11 (2018).
[4] M.-A. Miri and A. Alu, Exceptional points in optics and photonics, Science **363**, eaar7709 (2019).
[5] C. M. Bender and S. Boettcher, Real spectra in non-Hermitian Hamiltonians having $\mathcal{PT}$ symmetry, Phys. Rev. Lett. **80**, 5243 (1998).
[6] C. M. Bender, Making sense of non-Hermitian Hamiltonians, Rep. Prog. Phys. **70**, 947 (2007).
[7] H. Zhao and L. Feng, Parity-time symmetric photonics, Natl. Sci. Rev. **5**, 183 (2018).
[8] L. Feng, Z. J. Wong, R.-M. Ma, Y. Wang, and X. Zhang, Single-mode laser by parity-time symmetry breaking, Science **346**, 972 (2014).
[9] H. Hodaei, A. U. Hassan, S. Wittek, H. Garcia-Gracia, R. El-Ganainy, D. N. Christodoulides, and M. Khajavikhan, Enhanced sensitivity at higher-order exceptional points, Nature **548**, 187 (2017).
[10] Z. Lin, H. Ramezani, T. Eichelkraut, T. Kottos, H. Cao, and D. N. Christodoulides, Unidirectional invisibility induced by $\mathcal{PT}$-symmetric periodic structures, Phys. Rev. Lett. **106**, 213901 (2011).

[11] D. L. Sounas, R. Fleury, and A. Alù, Unidirectional cloaking based on metasurfaces with balanced loss and gain, Phys. Rev. Appl. **4**, 014005 (2015).
[12] X. Zhu, H. Ramezani, C. Shi, J. Zhu, and X. Zhang, $\mathcal{PT}$-symmetric acoustics, Phys. Rev. X **4**, 031042 (2014).
[13] C. Shi, M. Dubois, Y. Chen, L. Cheng, H. Ramezani, Y. Wang, and X. Zhang, Accessing the exceptional points of parity-time symmetric acoustics, Nat. Commun. **7**, 11110 (2016).
[14] T. Liu, X. Zhu, F. Chen, S. Liang, and J. Zhu, Unidirectional wave vector manipulation in two-dimensional space with an all passive acoustic parity-time-symmetric metamaterials crystal, Phys. Rev. Lett. **120**, 124502 (2018).
[15] X. Wang, X. Fang, D. Mao, Y. Jing, and Y. Li, Extremely asymmetrical acoustic metasurface mirror at the exceptional point, Phys. Rev. Lett. **123**, 214302 (2019).
[16] K. Stojanoska and C. Shen, Non-Hermitian planar elastic metasurface for unidirectional focusing of flexural waves, Appl. Phys. Lett. **120**, 241701 (2022).
[17] R. Cai, Y. Jin, Y. Li, J. Zhu, H. Zhu, T. Rabczuk, and X. Zhuang, Absorption-lasing effects and exceptional points in parity-time symmetric non-Hermitian metaplates, J. Sound Vib. **555**, 117710 (2023).
[18] L. Huang, S. Huang, C. Shen, S. Yves, A. S. Pilipchuk, X. Ni, S. Kim, Y. K. Chiang, D. A. Powell, and J. Zhu *et al.*, Acoustic resonances in non-Hermitian open systems, Nat. Rev. Phys. **6**, 11 (2024).
[19] S. Xia, D. Kaltsas, D. Song, I. Komis, J. Xu, A. Szameit, H. Buljan, K. G. Makris, and Z. Chen, Nonlinear tuning of PT symmetry and non-Hermitian topological states, Science **372**, 72 (2021).
[20] A. Stegmaier, S. Imhof, T. Helbig, T. Hofmann, C. H. Lee, M. Kremer, A. Fritzsche, T. Feichtner, S. Klembt, and S. Höfling *et al.*, Topological defect engineering and $\mathcal{PT}$ symmetry in non-Hermitian electrical circuits, Phys. Rev. Lett. **126**, 215302 (2021).
[21] Y. Li, C. Liang, C. Wang, C. Lu, and Y.-C. Liu, Gain-loss-induced hybrid skin-topological effect, Phys. Rev. Lett. **128**, 223903 (2022).
[22] B. Hu, Z. Zhang, H. Zhang, L. Zheng, W. Xiong, Z. Yue, X. Wang, J. Xu, Y. Cheng, and X. Liu *et al.*, Non-Hermitian topological whispering gallery, Nature **597**, 655 (2021).
[23] R. Pernas-Salomón, L.-Y. Zheng, Z. Zhang, P. Gao, X. Liu, Y. Cheng, and J. Christensen, Theory of non-Hermitian topological whispering gallery, npj Comput. Mater. **8**, 241 (2022).
[24] Y. Aurégan and V. Pagneux, $\mathcal{PT}$-symmetric scattering in flow duct acoustics, Phys. Rev. Lett. **118**, 174301 (2017).
[25] J. Christensen, M. Willatzen, V. Velasco, and M.-H. Lu, Parity-time synthetic phononic media, Phys. Rev. Lett. **116**, 207601 (2016).
[26] W.-J. Yang, Z.-Z. Yang, A.-Y. Guan, X.-Y. Zou, and J.-C. Cheng, Design and experimental demonstration of effective acoustic gain medium for PT-symmetric refractive index, Appl. Phys. Lett. **120**, 063503 (2022).
[27] L. Zhang, Y. Yang, Y. Ge, Y.-J. Guan, Q. Chen, Q. Yan, F. Chen, R. Xi, Y. Li, and D. Jia *et al.*, Acoustic non-Hermitian skin effect from twisted winding topology, Nat. Commun. **12**, 1 (2021).
[28] K. Wang, L. Shi, H. Zou, S. Zhao, C. Shen, and J. Lu, A broadband active sound absorber with adjustable absorption coefficient and bandwidth, J. Acoust. Soc. Am. **156**, 1048 (2024).
[29] R. Fleury, D. Sounas, and A. Alu, An invisible acoustic sensor based on parity-time symmetry, Nat. Commun. **6**, 5905 (2015).
[30] A. Maddi, V. Pagneux, and V. Achilleos, Exact analog of the Hatano-Nelson model in one-dimensional continuous nonreciprocal systems, Phys. Rev. Res. **6**, L012061 (2024).
[31] A. Szameit, M. C. Rechtsman, O. Bahat-Treidel, and M. Segev, $\mathcal{PT}$-symmetry in honeycomb photonic lattices, Phys. Rev. A **84**, 021806 (2011).
[32] Y. Benisty, S. Jana, and L. Sirota, Controlled wave acceleration in $\mathcal{PT}$-symmetric and inhomogeneous non-Hermitian lattices, Phys. Rev. B **111**, 174304 (2025).
[33] T. Hofmann, T. Helbig, C. H. Lee, M. Greiter, and R. Thomale, Chiral voltage propagation and calibration in a topolectrical Chern circuit, Phys. Rev. Lett. **122**, 247702 (2019).
[34] M. I. Rosa and M. Ruzzene, Dynamics and topology of non-Hermitian elastic lattices with non-local feedback control interactions, New J. Phys. **22**, 053004 (2020).
[35] T. Helbig, T. Hofmann, S. Imhof, M. Abdelghany, T. Kiessling, L. Molenkamp, C. Lee, A. Szameit, M. Greiter, and R. Thomale, Generalized bulk-boundary correspondence in non-Hermitian topolectrical circuits, Nat. Phys. **16**, 747 (2020).
[36] S. Jana and L. Sirota, Gravitational lensing and tunneling of mechanical waves in synthetic curved spacetime, Phys. Rev. Res. **5**, 033104 (2023).
[37] P. Zhu, X.-Q. Sun, T. L. Hughes, and G. Bahl, Higher rank chirality and non-Hermitian skin effect in a topolectrical circuit, Nat. Commun. **14**, 720 (2023).
[38] F. Langfeldt and J. Cheer, Controlling the effective surface mass density of membrane-type acoustic metamaterials using dynamic actuators, J. Acoust. Soc. Am. **153**, 961 (2023).
[39] X. Wen, H. K. Yip, C. Cho, J. Li, and N. Park, Acoustic amplifying diode using nonreciprocal Willis coupling, Phys. Rev. Lett. **130**, 176101 (2023).
[40] D. Halder, R. Thomale, and S. Basu, Circuit realization of a two-orbital non-Hermitian tight-binding chain, Phys. Rev. B **109**, 115407 (2024).
[41] S. Jana and L. Sirota, Invisible tunneling through non-Hermitian barriers in nonreciprocal lattices, Phys. Rev. B **111**, L100301 (2025).
[42] D. A. Kovacevich, K. Grosh, and B.-I. Popa, Stability-derived bounds on the realizable acoustic properties of active metamaterials, Phys. Rev. Appl. **21**, L051002 (2024).
[43] R. Chaunsali, C.-W. Chen, and J. Yang, Subwavelength and directional control of flexural waves in zone-folding induced topological plates, Phys. Rev. B **97**, 054307 (2018).
[44] E. Rivet, S. Karkar, and H. Lissek, Broadband low-frequency electroacoustic absorbers through hybrid sensor-/shunt-based impedance control, IEEE Trans. Control Syst. Technol. **25**, 63 (2016).
[45] N. Geib, A. Sasmal, Z. Wang, Y. Zhai, B.-I. Popa, and K. Grosh, Tunable nonlocal purely active nonreciprocal acoustic media, Phys. Rev. B **103**, 165427 (2021).
[46] The increase in the group velocity is due to the active metamaterial only and could not be due to temperature increase

or thermal expansion or contraction, as it would require a temperature of 46°C to explain, e.g., the measured increase of speed of sound at $\eta = 2$. Similarly, for plastics, the thermal expansion coefficient is approximately $80 \times 10^{-6}/^{\circ}$C, which would require very large temperature differences that were not possible in the laboratory.

[47] For a group velocity that is achieved, guaranteeing the stability in practice might require an additional control strategy, as the relation in Eq. 7 is based on an idealized assumption that all the circuit components in the metamaterial controller [see Fig. 2(b)], have the exact same values. In practice, the components might differ from each other in some percentage of their value, or their value might change during operation due to temperature increase, etc. The resulting balance would therefore be violated, leading to a possible instability.

[48] I. V. Lam, Analysis of improved Howland current pump configurations, Tex. Instrum. (2023).